Geophysical Journal International

Geophys. J. Int. (2017) **211,** 1062–1076
Advance Access publication 2017 August 19
GJI Seismology

doi: 10.1093/gji/ggx354

Toward automated directivity estimates in earthquake moment tensor inversion

Hsin-Hua Huang,[1,2,3] Naofumi Aso[2,4] and Victor C. Tsai[2]

[1]*Institute of Earth Science, Academia Sinica, Taipei* 115*, Taiwan. E-mail: hhhuang@earth.sinica.edu.tw*
[2]*Seismological Laboratory, California Institute of Technology, Pasadena, CA* 91125*, USA*
[3]*Department of Geology and Geophysics, University of Utah, Salt Lake City, UT* 84112*, USA*
[4]*Department of Earth and Planetary Science, The University of Tokyo, Bunkyo, Tokyo* 113-0033*, Japan. E-mail: aso@eps.s.u-tokyo.ac.jp*

Accepted 2017 August 18. Received 2017 July 13; in original form 2017 April 20

SUMMARY

Rapid estimates of earthquake rupture properties are useful for both scientific characterization of earthquakes and emergency response to earthquake hazards. Rupture directivity is a particularly important property to constrain since seismic waves radiated in the direction of rupture can be greatly amplified, and even moderate magnitude earthquakes can sometimes cause serious damage. Knowing the directivity of earthquakes is important for ground shaking prediction and hazard mitigation, and is also useful for discriminating which nodal plane corresponds to the actual fault plane particularly when the event lacks aftershocks or outcropped fault traces. Here, we propose a 3-D multiple-time-window directivity inversion method through direct waveform fitting, with source time functions stretched for each station according to a given directivity. By grid searching for the directivity vector in 3-D space, this method determines not only horizontal but vertical directivity components, provides uncertainty estimates, and has the potential to be automated in real time. Synthetic tests show that the method is stable with respect to noise, picking errors, and site amplification, and is less sensitive to station coverage than other methods. Horizontal directivity can be properly recovered with a minimum azimuthal station coverage of 180°, whereas vertical directivity requires better coverage to resolve. We apply the new method to the M_w 6.0 Nantou, Taiwan earthquake, M_w 7.0 Kumamoto, Japan earthquake, and M_w 4.7 San Jacinto fault trifurcation (SJFT) earthquake in southern California. For the Nantou earthquake, we corroborate previous findings that the earthquake occurred on a shallow east-dipping fault plane rather than a west-dipping one. For the Kumamoto and SJFT earthquakes, the directivity results show good agreement with previous studies and demonstrate that the method captures the general rupture characteristics of large earthquakes involving multiple fault ruptures and applies to earthquakes with magnitudes as small as M_w 4.7.

Key words: Earthquake ground motions; Earthquake source observations; Wave propagation.

1 INTRODUCTION

Rupture directivity is an important rupture property and is a primary characteristic of seismic source finiteness, with rupture propagation in a preferential direction (Haskell 1964). Although there is variability in the manner in which an earthquake ruptures on a fault plane (Wald & Heaton 1994; Beroza 1995; Ide & Takeo 1997; Yue *et al*. 2012; Ye *et al*. 2013), unilateral rupture is generally predominant in a wide range of earthquake magnitudes (McGuire *et al*. 2002; Tan & Helmberger 2010; Kane *et al*. 2013). As unilateral rupture occurs, seismic waves radiated in the direction of rupture could be greatly amplified, and even moderate magnitude earthquakes can sometimes cause serious damage (Huang *et al*. 2011; Kanamori *et al*. 2016). Knowing the directivity of earthquakes is therefore important for ground shaking prediction and in turn helps with hazard mitigation (Somerville *et al*. 1997; Spudich & Chiou 2008; Kurzon *et al*. 2014). Moreover, directivity can also be used to discriminate which nodal plane corresponds to the actual fault plane (Mori & Hartzell 1990; Warren & Shearer 2006; Frez *et al*. 2010). For moderate (and smaller) magnitude earthquakes and some large earthquakes that lack aftershocks or outcropped fault traces, such discrimination is particularly useful for better understanding fault structure at depth (Warren & Silver 2006; Chen *et al*. 2010).

Directivity is often discussed using the results of finite fault inversions (Kikuchi & Kanamori 1991; Yue *et al*. 2012; Ye *et al*. 2016) or back-projection techniques (Ishii *et al*. 2005; Koper *et al*. 2011;

Meng *et al*. 2011). Although these methods provide a spatiotemporal history of the rupture process, their application is mainly restricted to large earthquakes. More commonly, directivity for small-to-moderate earthquakes is estimated based on differences in source duration (Velasco *et al*. 1994; Tan & Helmberger 2010) or peak ground amplitude (Boatwright 2007; Convertito *et al*. 2012; Kurzon *et al*. 2014) observed between stations in the time domain, or differences in spectral ratios (Wang & Rubin 2011; Ross & Ben-Zion 2016) or corner frequencies (Kane *et al*. 2013) in the frequency domain. These studies convert observations of a single source parameter at each station to estimate directivity and therefore rely on a good azimuthal coverage of stations to resolve directivity since information at each station has been reduced to a single parameter. As data coverage and/or quality is often limited, a common *a priori* constraint of purely horizontal rupture propagation is often imposed to reduce the nonuniqueness of the problem. Park & Ishii (2015) noted the importance of directivity in the dip (vertical) direction and developed a two-step inversion method to estimate directivity in 3-D, but their method requires manual determination of apparent source duration and is not easy to be applied. Also, in the step of converting observations to a single parameter, most aforementioned studies rely on deconvolution by empirical Green's functions (EGFs) to remove path and site effects, for which deconvolution has been known to be not always stable, and perhaps more importantly, EGFs are not always available.

In this study, we propose a 3-D directivity moment tensor (DMT) inversion method to estimate earthquake rupture properties directly through waveform fitting without needing to individually estimate apparent source parameters (e.g. source duration, corner frequency) at each station. Assuming a continuous unilateral rupture, the apparent source time functions (ASTFs) observed at stations are simply stretched forms of the real source time function (RSTF) (Section 2). Such stretching can be determined according to a predefined directivity vector with respect to ray takeoff angle to each station. We can then grid search the directivity vector in 3-D space with different stretched source time functions to each station rather than a common source time function to all stations as is typical in moment tensor inversions (Dziewonski *et al*. 1981; Kanamori & Rivera 2008). In this manner, how properly the directivity effect is incorporated into the synthetic waveforms (convolution of Green's functions and stretched source time functions) relies on how precisely the RSTF is calculated. As the shape of the RSTF is never known in reality, the setting of multiple-time-windows (e.g. Aso & Ide 2014) is therefore key to determining the actual shape of the RSTF in the inversion. Fitting directivity using waveforms is also more constrained compared to only fitting by single source parameters (e.g. source duration) as in most of previous studies. Similar ideas based on source time function stretching has also been exploited recently (Zhan *et al*. 2015; Prieto *et al*. 2017). However, they still rely on EGF deconvolution to obtain ASTFs first before stretching them to search for directivity, which causes additional challenges for the more automated goal we have in mind.

Synthetic tests are performed to address possible effects of station distribution, background noise level, picking error, and site amplification (Section 3). Results show that in most cases the horizontal component of directivity can be resolved with a minimum azimuthal station coverage of 180°. The vertical component of directivity, however, requires better station coverage to resolve robustly. In Section 4, we then apply the method to the M_w 6.0 Nantou, Taiwan earthquake, M_w 7.0 Kumamoto, Japan earthquake, and M_w 4.7 San Jacinto fault trifurcation (SJFT) earthquake in southern California (Fig. 1), for which directivity is well documented (Lee *et al*. 2015; Ross & Ben-Zion 2016; Yagi *et al*. 2016). The directivity results obtained are in good agreement with previous studies and demonstrate the applicability of this method to a range of earthquake magnitudes. Because the directivity search (and corresponding stretching operation) is the only addition to typical waveform inversion, this one-step procedure is easily implemented and has the potential to be automated for real-time moment tensor monitoring systems (Tsuruoka *et al*. 2009; Ekstrom *et al*. 2012; Lee *et al*. 2013).

2 METHOD

2.1 Source time functions for a unilaterally propagating source

The quantitative description of directivity for a unilaterally propagating earthquake source has been described by many authors starting with Haskell (1964). However, despite the result that the ASTF at different azimuths are stretched in both amplitude and time depending on orientation relative to the rupture direction being intuitive, quantitative results appear explicitly in the literature only for sources with trapezoidal source time functions (e.g. Haskell 1964; Lay & Wallace 1995). Thus, for completeness, we derive the general result for an arbitrary source time function.

If an earthquake source is assumed to propagate unilaterally, its spatiotemporal source function (i.e. moment rate density function), $\dot{m}(t, \vec{\xi})$, can be expressed as a RSTF $\dot{M}(t)$ multiplied by a 3-D spatial delta function $\delta_{\xi}(\vec{\xi})$ associated with the rupture direction as

$$\dot{m}\left(t, \vec{\xi}\right) = \dot{M}\left(t\right) \delta_{\xi}\left(\vec{\xi} - \left(\overrightarrow{\xi_0} + \vec{v}t\right)\right), \tag{1}$$

where t is time, $\vec{\xi}$ denotes a spatial vector, $\overrightarrow{\xi_0}$ is the hypocenter, and $\vec{v}$ is a rupture velocity vector. Assuming that the source dimension is much smaller than the epicentral distance, the Green's functions for different locations of the propagating source share the same form except for a time offset so that

$$\vec{G}_j\left(\vec{\xi}; t\right) = \vec{G}_j\left(\vec{\xi}_0; t + \left(\vec{\xi} - \vec{\xi}_0\right) \cdot \vec{s}_j\right), \tag{2}$$

where $\vec{s}_j$ is a P- or S-wave slowness vector of the radiating (takeoff) ray to the station j around the source area. Using eqs (1) and (2), the observed velocity waveform $\vec{u}_j(t)$ at station j can then be written as

$$\begin{aligned}
\vec{u}_j\left(t\right) &= \int \dot{m}\left(t, \vec{\xi}\right) * \vec{G}_j\left(\vec{\xi}; t\right) \mathrm{d}\xi \\
&= \iint \dot{m}\left(\tau, \vec{\xi}\right) \vec{G}_j\left(\vec{\xi}; t - \tau\right) \mathrm{d}\xi \, \mathrm{d}\tau \\
&= \iint \dot{M}\left(\tau\right) \delta_{\xi}\left(\vec{\xi} - \left(\overrightarrow{\xi_0} + \vec{v}\tau\right)\right) \vec{G}_j \\
&\quad \times \left(\overrightarrow{\xi_0}; t - \tau + \left(\vec{\xi} - \overrightarrow{\xi_0}\right) \cdot \vec{s}_j\right) \mathrm{d}\xi \, \mathrm{d}\tau \\
&= \iint \dot{M}\left(\tau\right) \vec{G}_j\left(\overrightarrow{\xi_0}; t - \left(1 - \vec{v} \cdot \vec{s}_j\right)\tau\right) \mathrm{d}\tau.
\end{aligned} \tag{3}$$

By substituting $\tau = \tau'/(1 - \vec{v} \cdot \vec{s}_j)$, we obtain

$$\begin{aligned}
\vec{u}_j\left(t\right) &= \int \dot{M}\left(\tau' / \left(1 - \vec{v} \cdot \vec{s}_j\right)\right) \vec{G}_j\left(\overrightarrow{\xi_0}; t - \tau'\right) \mathrm{d}\tau' / \left(1 - \vec{v} \cdot \vec{s}_j\right) \\
&= \frac{\dot{M}\left(t / \left(1 - \vec{v} \cdot \vec{s}_j\right)\right)}{\left(1 - \vec{v} \cdot \vec{s}_j\right)} * \vec{G}_j\left(\overrightarrow{\xi_0}; t\right),
\end{aligned} \tag{4}$$

which shows that the only difference between the observed velocity waveform for a unilaterally propagating source and that for a point source is that the source time function is stretched in both time and amplitude due to the (3-D) directivity effect (resulting in the ASTF).

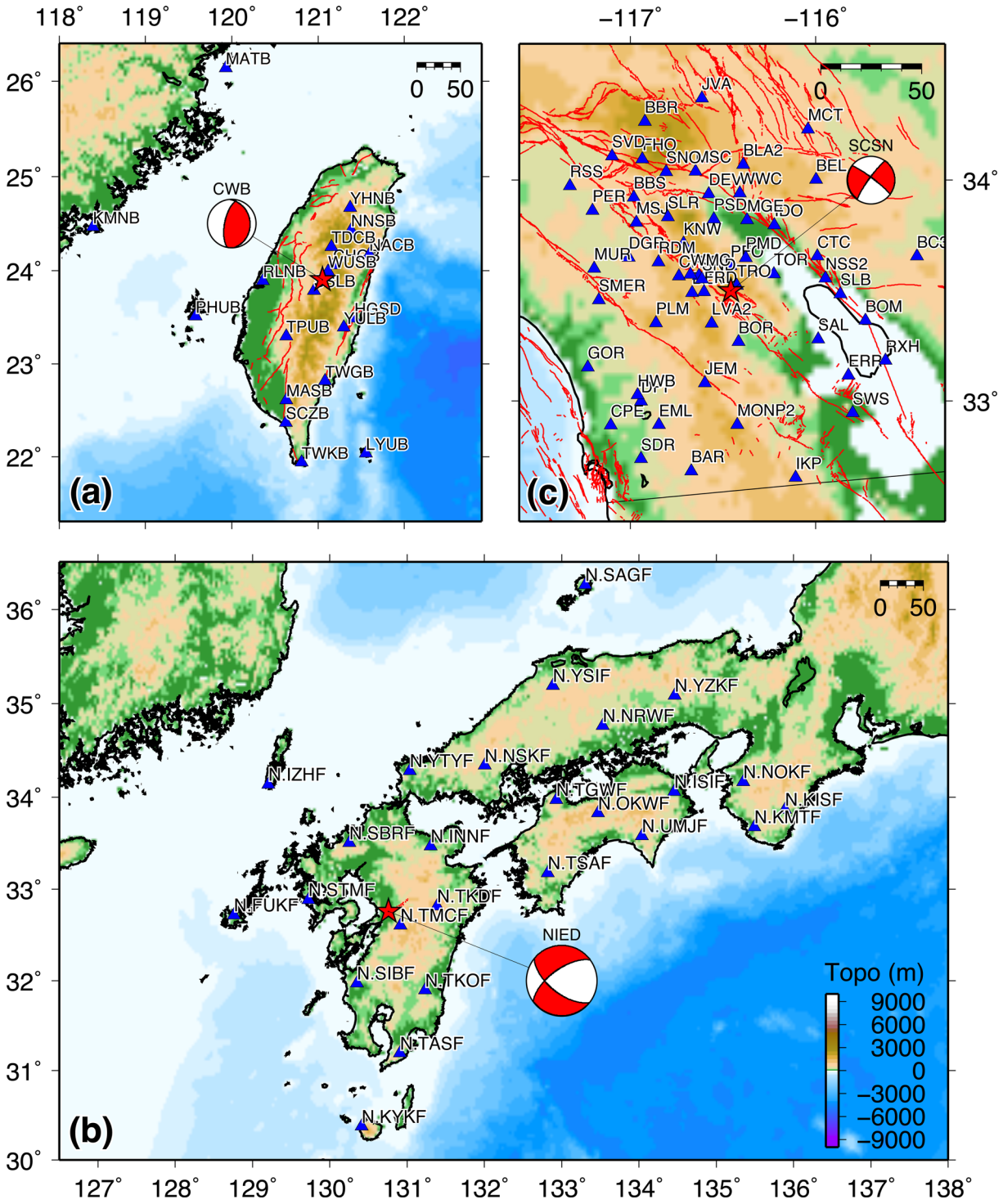

Figure 1. Hypocenter, focal mechanism, and station distribution for (a) the M_w 6.0 Nantou earthquake in central Taiwan, (b) the M_w 7.0 Kumamoto earthquake in Kyushu, Japan, and (c) the M_w 4.7 San Jacinto fault trifurcation earthquake in southern California, USA. The red lines and stars indicate fault traces and hypocenters. The blue triangles denote the stations used and are labeled with station names. The local agencies issuing the focal mechanisms are denoted above the beach balls: CWB, Central Weather Bureau (Taiwan); NIED, National Research Institute for Earth Science and Disaster Resilience (Japan); and SCSN, Southern California Seismic Network (United States).

This derivation naturally results in the preservation of source time function area as is often assumed in previous studies (Lay & Wallace 1995; Tan & Helmberger 2010), as shown by the red curves relative to blue curve in Fig. 2.

2.2 Introduction of the multiple-time-window representation

Eq. (4) allows us to model the apparent (stretched) source time functions of a unilateral propagating source by simply using the

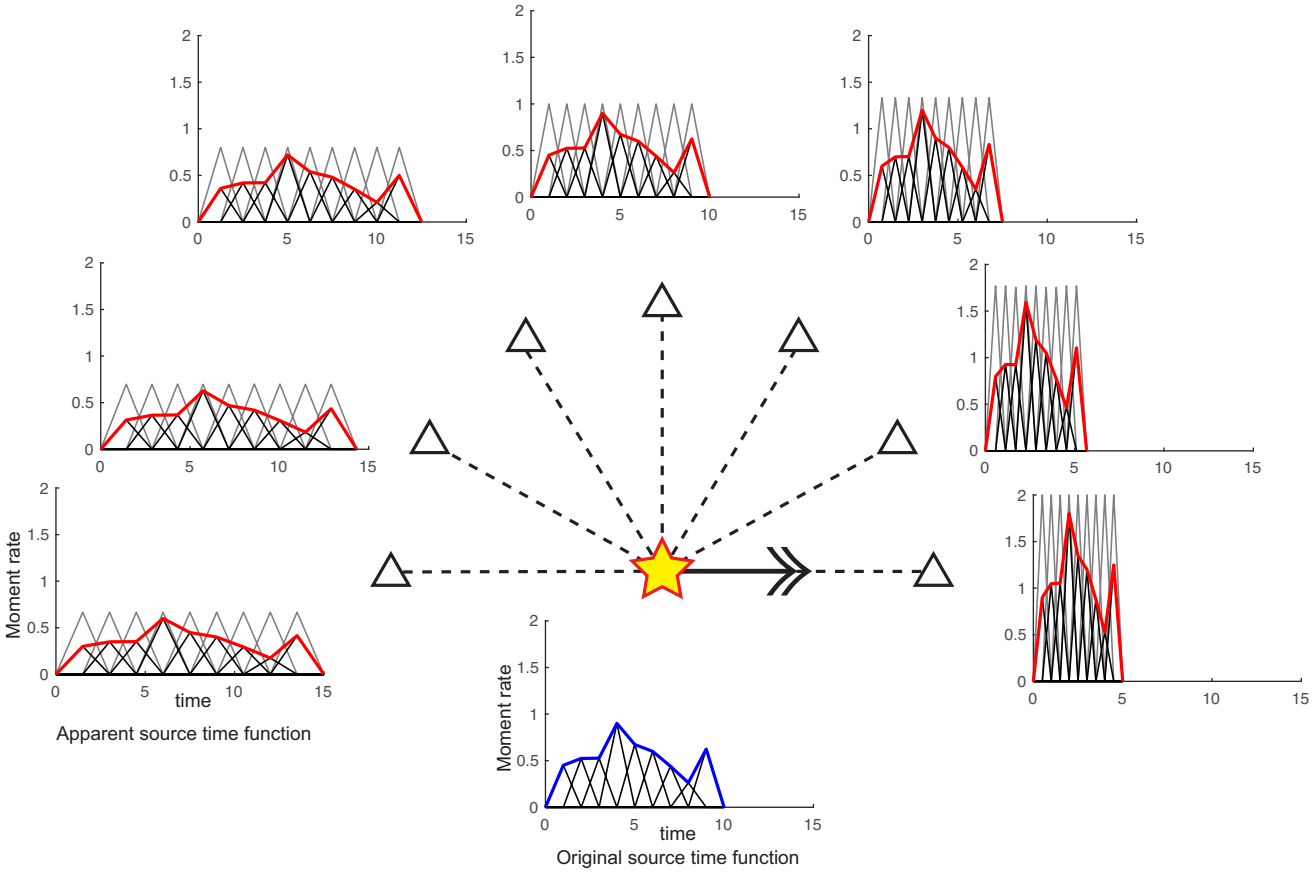

Figure 2. Schematic plot for multiple-time-window directivity inversion. As an earthquake ruptures from its epicenter (yellow star) horizontally to the east (black arrow), the real source time function (RSTF, blue curve) recorded at stations (bold triangles) will vary with azimuth with respect to the rupture direction due to directivity effects (red curves). The stretched multiple-time-windows (gray triangles) are therefore designed to capture such variations in source time functions (i.e. apparent source time functions, ASTFs) through our directivity inversion (black triangles). The dashed lines represent the rays emitted from the epicenter to each station in map view. The horizontal and vertical axes of the source time functions represent time and moment rate, respectively.

point-source source time function and Green's function. However, the real point-source source time function is always unknown and could be complicated (blue curve in Fig. 2). Utilizing a multiple-time-window strategy that is commonly used in finite fault inversion (Olson & Apsel 1982; Lee *et al*. 2006), we assume the point-source source time function to be composed of multiple basis functions as

$$\dot{M}(t) = \sum_i M_i f_i(t),$$

where $f_i(t)$ is the ith basis function that satisfies

$$\int f_i(t)\,\mathrm{d}t = 1$$

and M_i is the corresponding moment. As shown by grey triangles in Fig. 2, we use half overlapping triangular functions as our basis functions. Eq. (4) then becomes

$$\vec{u}_j(t) = \sum_i M_i \left[\frac{f_i\left(t/\left(1-\vec{v}\cdot\vec{s}_j\right)\right)}{1-\vec{v}\cdot\vec{s}_j} * \vec{G}_j(\vec{\xi_0};t) \right], \qquad (5)$$

which is a linear inverse problem for M_i (black triangles), and which models the actual shape of the source time functions (red curves in Fig. 2).

2.3 Directivity inversion procedure

To implement the multiple-time-window directivity inversion, we first conduct an ordinary moment tensor inversion to obtain a point-source moment tensor solution using the method of Aso & Ide (2014); if focal mechanisms from previous studies are available, those mechanisms could be used and this step could be skipped. Next, for any given rupture velocity vector $\vec{v}$, the basis functions are stretched (and shifted) according to eq. (5) and convolved with Green's functions for the obtained moment tensor solution to generate synthetic waveforms that incorporate the directivity effect. We then grid search the directivity vector (i.e. rupture velocity vector) in 3-D space with a non-negative least-squares inversion to determine the moments of each basis function simultaneously through direct waveform fitting of the observations. The amplitudes of the multiple basis functions determine the shape of the source time function. The optimal directivity is then determined by the directivity with maximum variance reduction of the waveform misfits, where waveform misfit is defined as $1-\frac{\sum_i (d_i-s_i)^2}{\sum_i d_i^2}$, where d and s are the observed and simulated waveforms, and i denotes the samples within the selected time window. We choose this two-step inversion rather than a one-step joint inversion (i.e. inverting for moment tensor and directivity together) mainly because different frequency bands are optimal for the two steps. The directivity inversion needs a relatively higher frequency band to be more accurately implemented; thus, combining

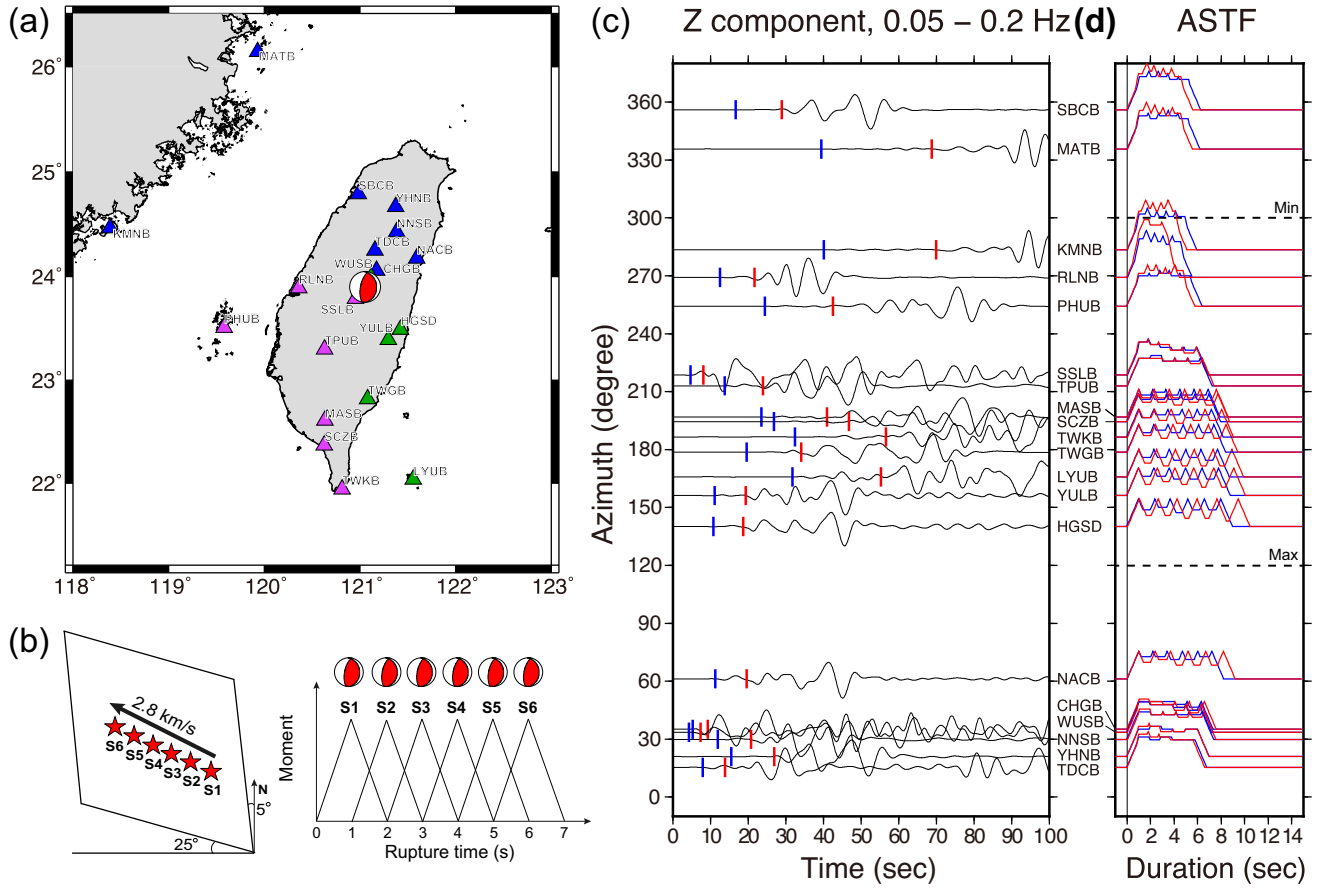

Figure 3. Setup of synthetic tests based on the actual station distribution and source parameters of the M_w 6.2 Nantou earthquake in central Taiwan. (a) The stations (triangles) used for the scenario Ideal (blue+purple+green), Gap180 (purple+green), and Gap270 (purple) (Table 1). (b) Schematic 3-D geometry and source time function for a linear source simulated by six subevents. The red stars represent the six subevents (S1–S6) that occurred linearly on the fault plane in a propagation direction denoted by the black arrow, and with a speed of 2.8 km s^{-1}. The occurrence times and source durations of the six subevents are represented by six triangle basis functions in the time–moment plot. Focal mechanisms of the subevents are shown above the basis functions and are assumed to be identical. (c) The synthetic waveforms at different stations as a function of azimuth. Station names are labeled to the right of each trace. The blue and red bars denote the *P*- and *S*-wave arrivals. (d) *P*-wave (blue) and *S*-wave (red) apparent source time functions (ASTFs) at different stations as a function of azimuth. The minimum and maximum apparent durations are marked by dotted lines based on rupture azimuth.

the two steps into one results in derived focal mechanisms that are not as stable as those derived using a lower frequency band. Thus, our preferred strategy is to use a lower frequency band to determine the focal mechanism first and then to fix the focal mechanism to subsequently search the directivity vector using a higher frequency band.

3 SYNTHETIC TESTS

For the sake of comparing with actual data later, here we adopt the station distribution and source parameters from the M_w 6.0 Nantou earthquake which occurred on 2013 March 27, in central Taiwan for the synthetic tests. As shown in Fig. 3a, 20 stations from the Broadband Array in Taiwan for Seismology (BATS) are used and have good azimuthal coverage of the epicentral area. Based on previous studies (Lee *et al*. 2015), the strike, dip, and rake of the Nantou earthquake are 355°, 25°, 75°, respectively, and it had a strong west-northwestward directivity. To mimic this directivity, we simulate a linear source which consists of 6 point-source subevents at 1 s intervals, each with a triangular source time function of 2 s duration and with propagation in the direction 300°E of N along the fault plane (Fig. 3b). Total source duration is therefore 7 s. A rupture velocity of 2.8 km s^{-1} is assumed and used to determine locations of the subevents along the assigned directivity direction. Using the F-K package (Zhu & Rivera 2002), synthetic waveforms with a sampling rate of 0.1 Hz for each subevent are generated and then summed to produce the final synthetic data representative of the linear propagating source (Fig. 3c). By shifting the triangular source time functions of each subevent according to arrival times from each subevent to each station, we can model the ASTFs for *P* and *S* waves observed at each station, respectively (Fig. 3d). It is worth noting that the *P*- and *S*-wave ASTFs show different levels of variations. Because of the slowness term (around the source area) in eq. (5), *S* waves always suffer stronger directivity effects than *P* waves do.

For the inversion, we first use a 7-s-duration triangular function to perform the ordinary moment tensor inversion at a lower frequency band of 0.02–0.05 Hz. The obtained fault plane solution is 338°, 17° and 61° in strike, dip and rake, which are in good agreement with our input solution (Fig. 4a). Note that the existence of directivity in this case prevents the solution from being perfectly recovered. Next, we fix the obtained moment tensor solution and set up seven triangular basis functions of 2-s duration (half overlapping) for the

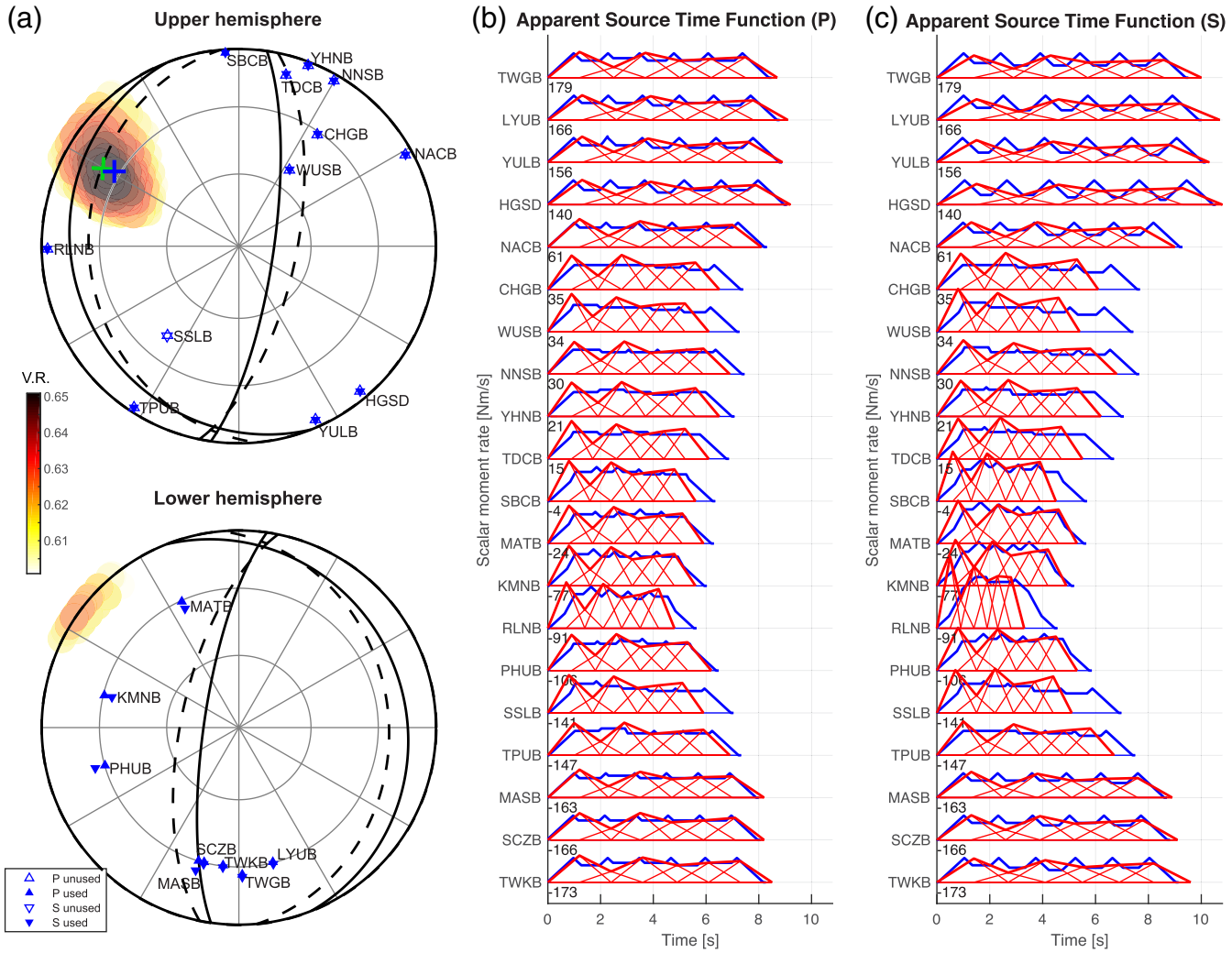

Figure 4. Inversion results of the synthetic test (Ideal scenario). (a) Directivity results shown in upper and lower hemispheres. Normal and inverted triangles represent *P*- and *S*-wave radiation (takeoff) angles corresponding to each station. Closed and open triangles denote the waveforms used and not used (based on the criteria), respectively. The input (true) focal planes and directivity are indicated by dashed black lines and a green cross. Reddish colors represent variance reduction (V.R.) and the best solution is denoted by a blue cross. Apparent source time functions for the input model (blue) and output results (red) at different stations for (b) *P* waves and (c) *S* waves, respectively. Stations are sorted according to azimuth.

multiple-time-window directivity inversion at a higher frequency band of 0.05–0.15 Hz. This higher frequency band is necessary for the directivity inversion since directivity effects are less obvious at the lower frequencies. The optimal directivity estimate is at 301.0° in azimuth and −27.2° in plunge. These values are very close to the input parameters (300° and −25°) although the rupture velocity of ∼2.62 km s^{-1} is slightly underestimated (Fig. 4a). While the recovery of the vertical component of rupture directivity has been long known to be a difficult challenge and poorly determined, it is encouraging that we obtain the correct up-dip direction in this synthetic inversion without any *a priori* constraint imposed. The estimated *P*- and *S*-wave ASTFs at the stations also match quite well with the synthetic source time functions through the multiple-time-window setting (Fig. 4b and c). This directivity effect is clearly reflected in the waveforms and cannot be modeled by the ordinary moment tensor inversion, for example, at the stations (e.g. RLNB) in the direction of directivity (Fig. 5).

The variance reductions before and after directivity inversion are 43.7 and 65.1 per cent, respectively. Although the variance reduction is improved, it is still quite low for a noise-free synthetic test (see 'Ideal' scenario in Table 1). This could be ascribed to several causes: (1) the linear source we simulate is made up of six subevents and not a continuous rupture as assumed in our mathematical description; (2) the identical Green's functions assumption made for a moving source is not precise at such a regional scale; (3) the imperfect determination of the focal mechanism in the first step inevitably introduces error into the second step of the directivity inversion to some extent; (4) the change of radiation (takeoff) angle during the source propagation is not considered in the current mathematical formulation; for example, polarity could change sign during the rupture propagation for some stations located near the nodal plane of the focal mechanism; and (5) multiple phases such as the *Pnl* wave train (Helmberger & Engen 1980) that follow direct *P* at regional distances but have different directivity effects (due to different ray paths) also increase the misfits. However, we stress that even though such issues exist, directivity can still be successfully recovered, which implies that the method can tolerate modeling errors.

We further test scenarios involving different levels of background noise levels, picking time errors, site amplification and gap angles (i.e. station distribution), as summarized in Table 1. In the scenarios

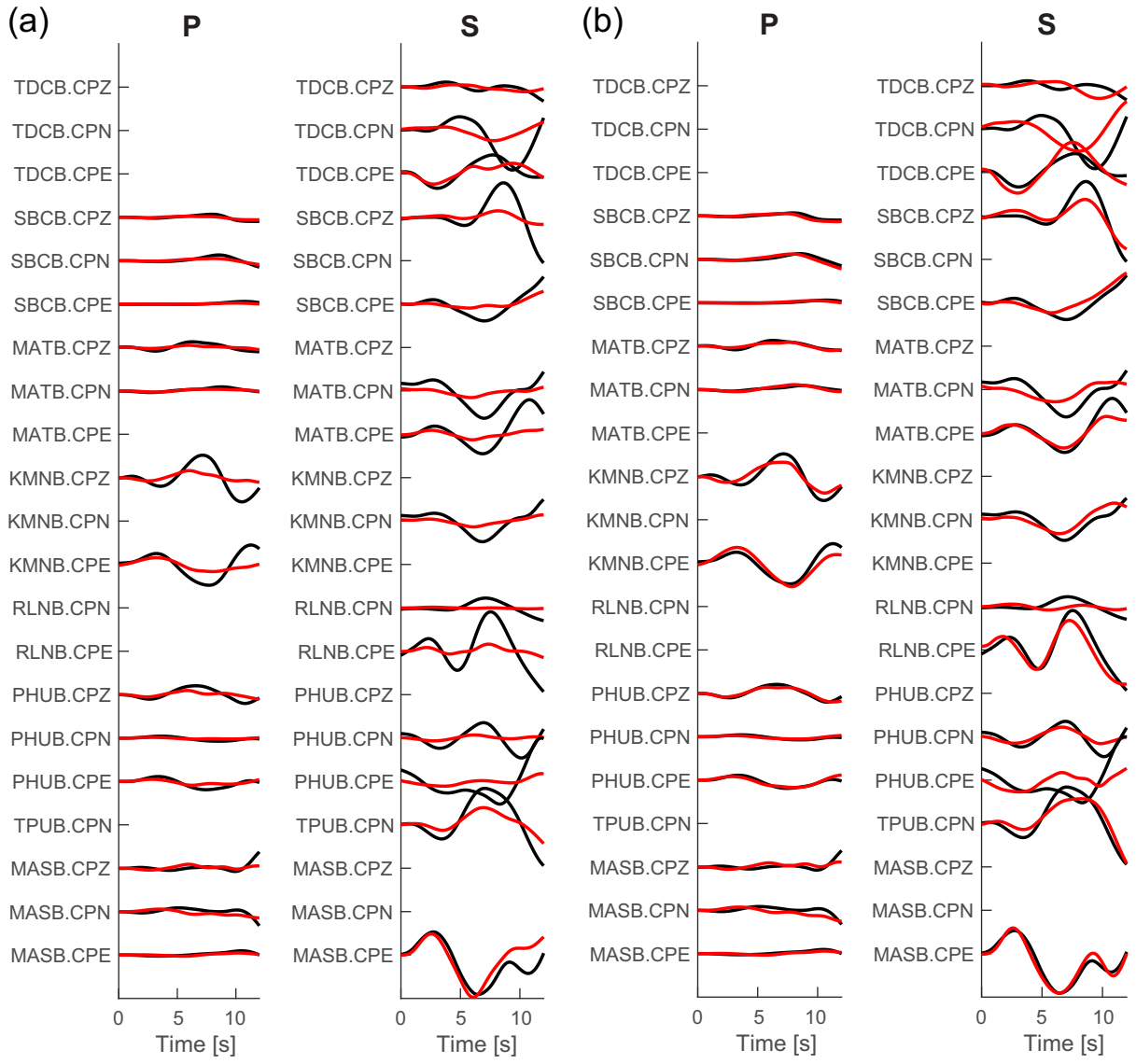

Figure 5. Comparison of three-component *P*- and *S*-wave waveform fits for the synthetic test (Ideal scenario) at selected stations between (a) the ordinary moment tensor inversion and (b) the DMT inversion. Black lines are input synthetic waveforms and red lines are the synthetic waveforms reproduced from the inversion results. The channel name CP refers to the composite synthetics we produced.

Noise1 and Noise2, random noise with a zero mean and standard deviations that are 5 and 10 per cent high of the peak value of synthetics are added individually to each station. In the scenarios Picking1 and Picking2, random time shifts with a zero mean and standard deviations of 0.5 and 1.5 s are generated and added in the *P*- and *S*-wave time windows separately for inversion. In scenarios Site1 and Site2, a random amplification factor, α, with a zero mean and a standard deviation of 0.5 and 1.0 is generated. We then randomly amplify (multiply) the synthetics by a factor of $(1 + \alpha)$ for all three components. Finally, in scenarios Gap180 and Gap270, we test two station distributions with a gap angle of 180° (green and purple stations in Fig. 3a) and 270° (purple stations in Fig. 3a), respectively. The effect of 3-D (velocity) heterogeneity has analogously been considered with the scenarios involving picking time errors and site amplification. The frequency bands used and the inversion procedures are identical as aforementioned.

Results show that the focal mechanism is almost unaffected for all scenarios but always slightly biased because of the directivity effect. This explains why ordinary moment tensor inversion is quite robust with only simple 1-D models (for a low frequency band) but also implies that solutions using typical frequency bands (0.02–0.05 Hz) at a regional scale could be biased if the source is not purely a point source. Moreover, horizontal directivity can be determined robustly as long as the station distribution is not too poor (gap angle larger than 180°). Once the gap angle is larger than 180°, the horizontal directivity estimates start to deviate. In contrast, vertical directivity is, perhaps not surprisingly, less robust and requires better azimuthal station coverage to resolve. Noise level and station coverage seem to affect vertical directivity the most. Nonetheless, we note that all the results give the correct up-dip direction. Rupture velocity, on the other hand, is always stable but underestimated. We will discuss reasons for this underestimate later in Section 5. In terms of variance reduction, picking time errors seem to be one of the key controlling factors that worsen the fits; the reasons for the high variance reductions (up to 80–90 per cent) of scenarios Gap180 and Gap270 are simply because worse azimuthal station coverage causes

Table 1. Summary of the synthetic tests for scenarios involving different levels of background noise, picking time errors, site amplification, and gap angles. See main text for more details. V.R. is variance reduction.

	Focal mechanism			Directivity			
Scenario	Strike (°)	Dip (°)	Rake (°)	Azimuth (°)	Plunge (°)	Velocity (km s^{-1})	V.R. (%)
Input	355	25	75	300.0	−25.0	2.8	
Ideal	338	17	61	300.9	−27.2	2.6	65.1
Noise1	338	16	62	299.7	−36.6	2.0	65.4
Noise2	337	16	61	293.2	−46.4	2.2	64.1
Picking1	338	16	61	299.7	−31.8	1.9	53.6
Picking2	341	16	62	299.1	−21.2	2.2	33.1
Site1	343	17	66	300.9	−23.2	2.5	63.3
Site2	345	17	68	299.1	−21.2	2.2	61.6
Gap180	349	21	66	296.6	−5.1	2.2	80.2
Gap270	351	19	64	288.4	−40.1	2.5	88.9

smaller waveform differences between stations (due to directivity) so that it is easier to achieve good waveform fits, which, however, are not necessarily correct. Variance reduction should therefore not be taken as the only standard to judge the quality of solutions.

4 APPLICATIONS AND RESULTS

In this section, the method is applied to three earthquakes with moment magnitude ranging from 4.7 to 7.0 to test and demonstrate its stability and applicability. The three earthquakes are the M_w 6.0 Nantou earthquake in central Taiwan, the M_w 7.0 Kumamoto earthquake in Kyushu, Japan, and the M_w 4.7 SJFT earthquake in southern California, respectively (Fig. 1). The waveform data are downloaded from BATS, the National Research Institute for Earth Science and Disaster Resilience (NEID) F-net and the Southern California Earthquake Data Center (SCEDC) for the Nantou, Kumamoto and SJFT earthquakes, respectively. The data sampling rates are 40 Hz for the SJFT earthquake and 100 Hz for the other two. All seismograms are velocity seismograms and are demeaned and detrended, with instrument response removed, and down-sampled to 10 Hz for the following analysis. To define the time windows used for inversion, we use the catalog picks from the SCEDC for the San Jacinto Fault earthquake, and manually pick the arrivals for the Nantou and Kumamoto earthquakes. Representative local 1-D velocity models for Taiwan (Chen 1995), Japan (Ueno *et al*. 2002) and southern California (Hadley & Kanamori 1977) are used for computing synthetics.

4.1 M_w 6.0 Nantou, Taiwan earthquake

On 2013 March 27, a M_w 6.0 (M_L 6.2) earthquake struck Nantou County in central Taiwan. This earthquake has been interpreted to occur on an east-dipping ramp fault system that ramps up on a strong basement high in the west and connects to the Chelungpu fault at shallow depths (Chuang *et al*. 2013; Lee *et al*. 2015), or on a preexisting rift-related extensional fault of the Hsuehshan Basin steeply dipping to the west (Camanni *et al*. 2014). Finite fault analysis shows a strong west-northwestward and up-dip directivity with a rupture velocity of ∼2.8 km s^{-1} but the east-dipping fault plane is presumed (Lee *et al*. 2015). Using our method, we are able to reexamine this structural ambiguity by searching for the directivity direction in 3-D space without assuming a fault plane.

Inversion parameters (e.g. frequency band) are almost the same as those used in synthetic tests except we use longer duration basis functions (4 s) for the actual data. Using shorter duration basis functions does not change the directivity results much but we obtain a source time function that is not as smooth in this case (Fig. 6b). The results show a focal mechanism of 352°, 23° and 78° in strike, dip and rake, consistent with previous studies (Lee *et al*. 2015). An estimated northwestward and up-dip directivity with an azimuth of 303.7° and a plunge of −29° matches the east-dipping fault plane and corroborates its occurrence on a ramp fault system rather than on a rift-related extensional fault (Fig. 6a). The source time function is determined to be about 6 s with an asymmetrical shape with a peak at 2 s and gently decreasing afterward. These primary features of our source time function are also consistent with the results from finite fault analyses (Lee *et al*. 2015).

4.2 M_w 7.0 Kumamoto, Japan, earthquake

We also test our method with the Kumamoto earthquake (M_w 7.0), which occurred on 2016 April 15 (UTC). Preceded by a foreshock (M_w 6.0) occurring on the Hinagu fault 28 hr before, the mainshock rupture initiated on the Hinagu fault and propagated north-northeast toward the Futagawa fault (Asano & Iwata 2016; Kubo *et al*. 2016; Yagi *et al*. 2016). The average rupture velocity was around 2.4 km s^{-1} in the north-northeast direction (Asano & Iwata 2016; Yagi *et al*. 2016). Since the Kumamoto earthquake is a relatively large event, to better satisfy the plane wave assumption, we use stations at a larger distance within 500 km from the epicenter (Fig. 1b). A total of 25 stations are then used. Since surface waves contaminate the *S*-wave time windows at these epicentral distances, we use only *P* waves in this case.

The frequency bands used for the first step of ordinary moment tensor inversion and the second step of directivity inversion are 0.01–0.04 Hz and 0.04–0.1 Hz, respectively. The basis function durations are set to 6 s. The obtained strike, dip, and rake are 232°, 70°, and 227° and agree with those from other agencies (Fig. 9). The directivity direction is estimated to be N4.1°E, which is slightly off from the strike of the Futagawa fault (Fig. 7). However, we emphasize that the Kumamoto earthquake is a relatively large earthquake with complex ruptures across multiple fault segments (Asano & Iwata 2016; Kubo *et al*. 2016; Yagi *et al*. 2016). As a primary estimate, our method well resolves the average behavior of the rupture and provides reasonable and rapid results critical for hazards estimates.

4.3 M_W 4.7 SJFT earthquake in the southern California

With the aim of testing the lower magnitude limit of our method in this section, we select the 2013 March 11 M_w 4.7 earthquake which occurred in the SJFT region of southern California, for which a strong northwestward directivity has been reported in previous studies (Kurzon *et al*. 2014; Ross & Ben-Zion 2016). As the Southern California Seismic Network is dense, we only use stations within an epicentral distance of 100 km for analysis (Fig. 1c), which results in 56 stations. The frequency bands we use are 0.05–0.15 and 0.15–0.5 Hz for the moment tensor and the directivity inversions, and 0.8-s duration basis functions are used in this case. A higher frequency band needs to be used to resolve the directivity of a smaller magnitude event. Although imperfect 1-D velocity models often prevent the use of high frequency signals, one can always use more sophisticated 3-D models or EGFs instead.

Consistent results for focal mechanism and northwestward directivity are obtained from our inversion, showing the actual fault plane in the NW-SE direction (Figs 8 and 9). The wider spread of

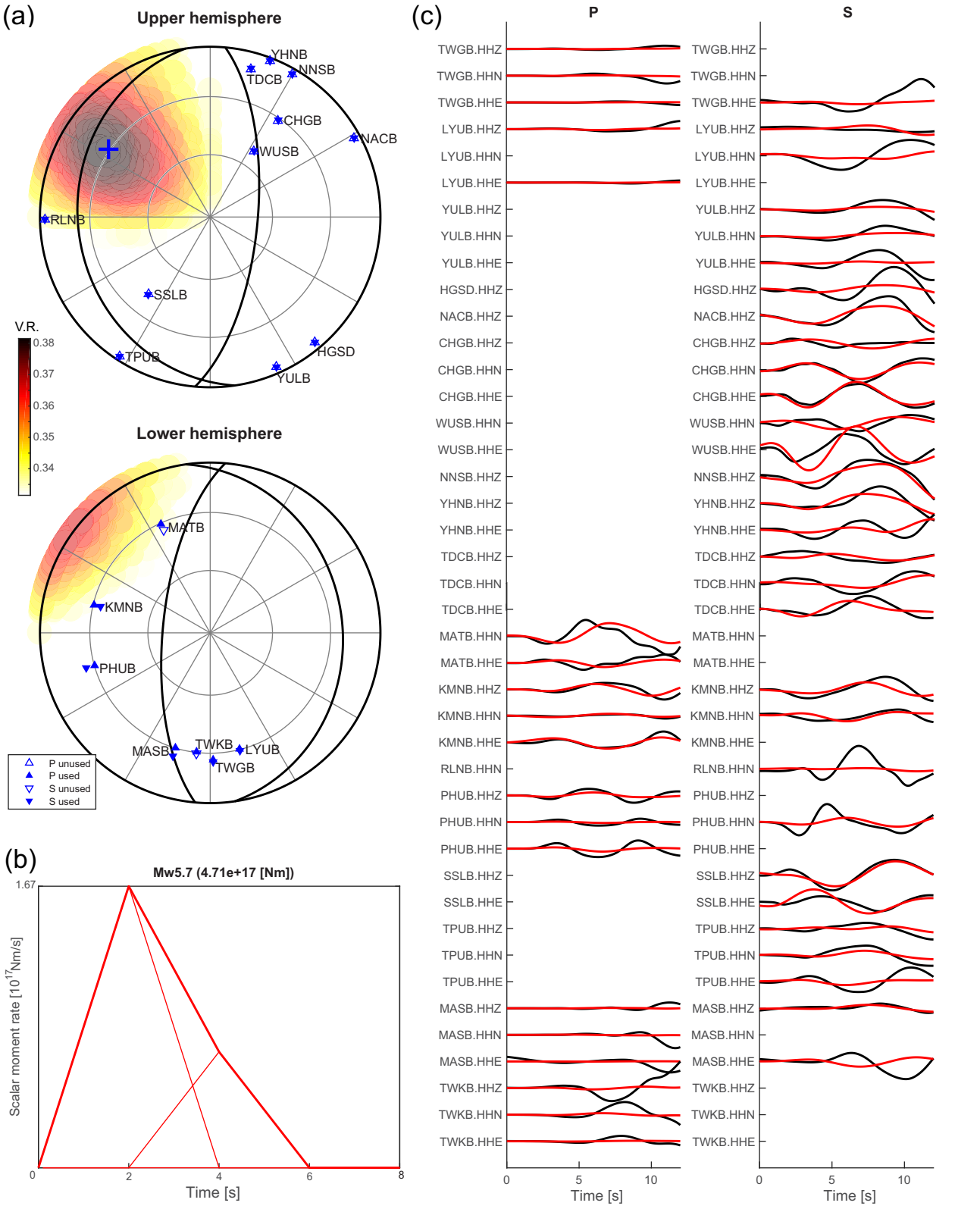

Figure 6. Inversion results for the M_w 6.0 Nantou earthquake. (a) Directivity results shown in upper and lower hemispheres. The blue cross and background colors denote the optimal directivity solution and variance reduction (V.R.). Refer to Fig. 4(a) for detailed annotations. (b) Inverted source time function. Red thick curve and red thin-line triangles indicate the overall function and the basis functions, respectively. (c) Three-component waveform fits for the *P*- and *S*-wave windows. The black and red curves are data and synthetic waveforms, respectively, with station names and channels on the left.

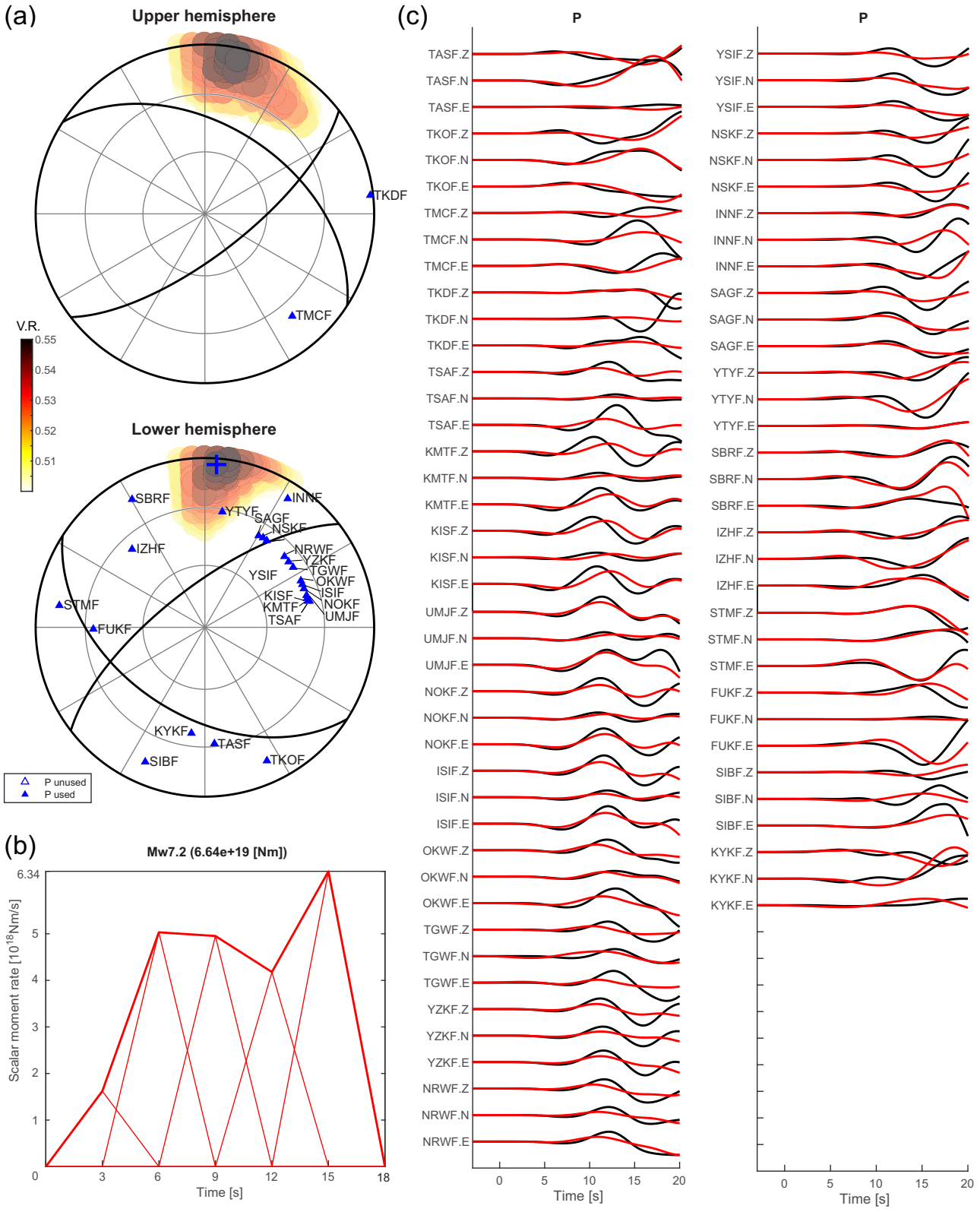

Figure 7. Inversion results for the M_w 7.0 Kumamoto earthquake. (a) Directivity results shown in upper and lower hemispheres. (b) Inverted source time function. (c) Three-component waveform fits for *P*- and *S*-wave windows. Refer to Fig. 6 for detailed annotations.

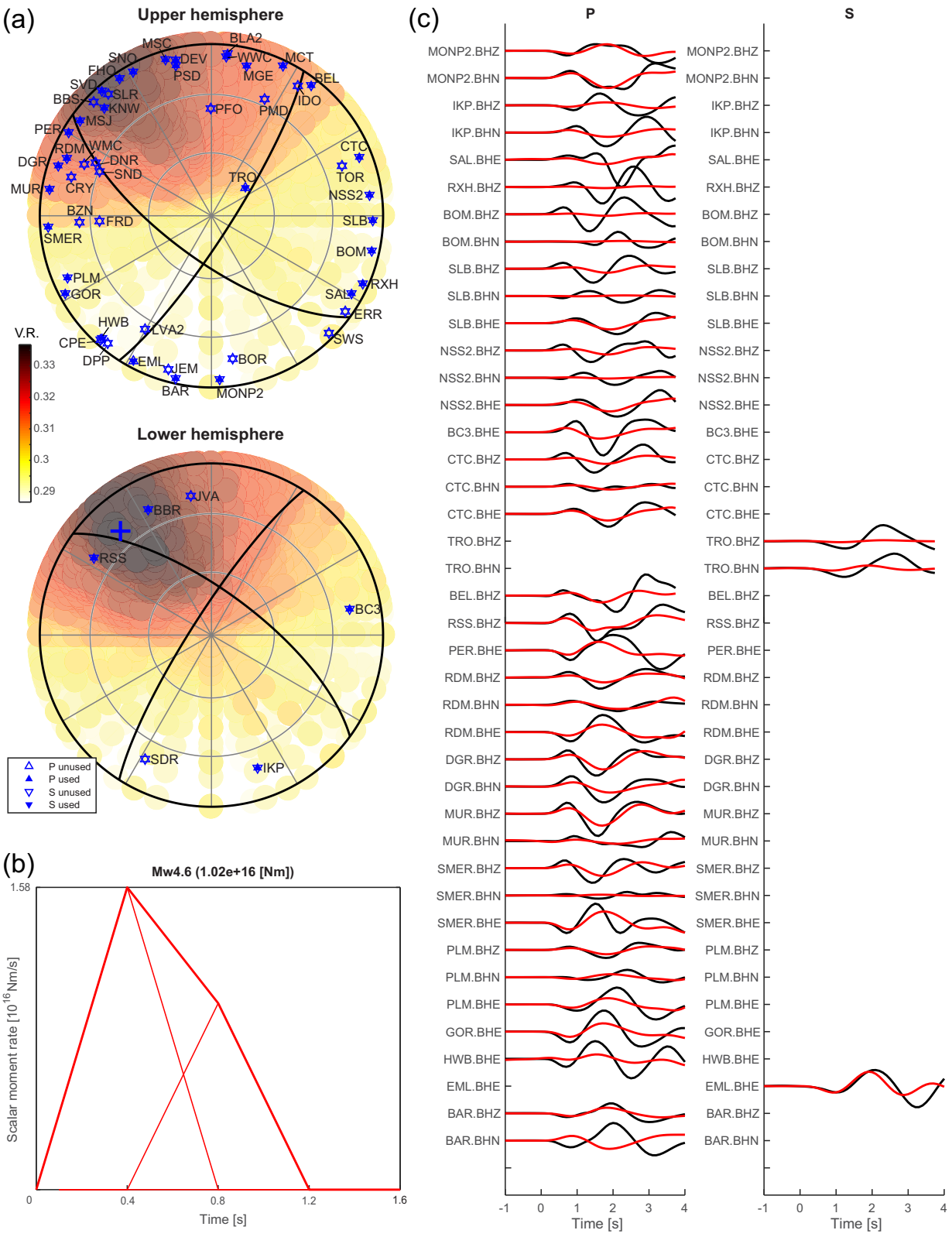

Figure 8. Inversion results for the M_w 4.7 San Jacinto fault trifurcation earthquake. (a) Directivity results shown in upper and lower hemispheres. (b) Inverted source time function. (c) Three-component waveform fits for *P*- and *S*-wave windows. Refer to Fig. 6 for detailed annotations.

directivity estimates on the focal sphere mainly results from the limitations of an imperfect 1-D velocity model for generating the high-frequency synthetics used and the lower signal-to-noise ratio in the data for a smaller magnitude event (Fig. 8a).

5 DISCUSSION AND CONCLUSIONS

Here we have introduced a general-purpose automated methodology for rapidly estimating the primary earthquake rupture properties by

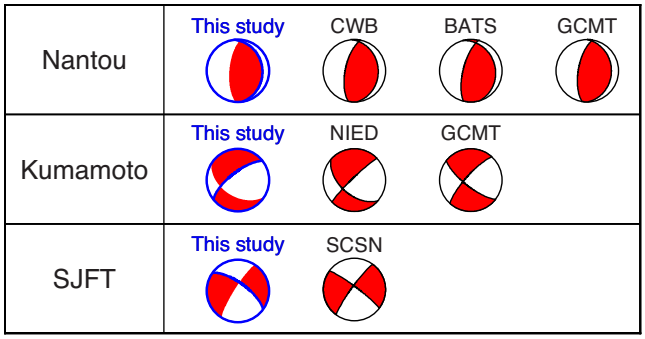

Figure 9. Comparison of focal mechanisms obtained in this study and issued by other agencies. CWB, Central Weather Bureau; BATS, Broadband Array in Taiwan for Seismology; GCMT, Global Centroid Moment Tensor Catalog; NIED, National Research Institute for Earth Science and Disaster Resilience; and SCSN, Southern California Seismic Network. The primary fault plane is identified by the directivity direction and marked in blue.

Table 2. Summary of the directivity inversion results applied to the three targeted earthquakes. See main text for more details on individual events. V.R. is variance reduction.

	Focal mechanism			Directivity				
Event	Strike (°)	Dip (°)	Rake (°)	Azimuth (°)	Plunge (°)	Velocity (km s^{-1})	M_W	V.R. (%)
Nantou	352	23	78	303.7	−29.0	2.5	5.7	38.2
Kumamoto	232	70	−133	4.1	4.1	2.8	7.2	55.0
SJFT	306	69	−170	318.8	20.6	2.3	4.6	33.7

direct waveform fitting with source time function stretching based on an assumption of unilateral propagation. The rupture direction (i.e. directivity) is the main parameter of interest and offers a rapid assessment of potential ground shaking amplification. Furthermore, it helps distinguish the actual fault plane from the auxiliary one, and also provides rupture velocity and source duration, by which the rupture length and stress drop could also be estimated. Based on our inversion results (Figs 6–8; Table 2), we obtain a unilateral rupture length of 15.0, 50.4, and 2.8 km for the M_W 6.0 Nantou earthquake, M_W 7.0 Kumamoto earthquake, and M_W 4.7 SJFT earthquake, respectively. Following Kanamori & Anderson (1975) and assuming a crust with a Poisson's ratio of 0.25 (Aki 1966), we can then estimate the stress drop for a dip-slip rectangular fault as

$$\frac{8}{3\pi}\frac{M_0}{w^2 L}, \tag{6}$$

and for a strike-slip one as

$$\frac{2}{\pi}\frac{M_0}{w^2 L}, \tag{7}$$

where w, L, and M_0 are the fault width and length, and seismic moment, respectively. Although fault width cannot be directly obtained via our method, we could assume it approximately scales with fault length following a well-established empirical relationship, $w = 1.7L^{2/3}$, for $5.5 < L < 1500$ km (Leonard 2010). Fault width is assumed equal to fault length if $L < 5.5$ km. Also, it has long been recognized that strike-slip earthquakes become width-limited at widths of 12–20 km; for strike-slip events with $w > 15$ km, we fix the width to 15 km (i.e. the average seismogenic depth; Leonard 2010). Therefore, the fault width for the Nantou earthquake, the Kumamoto earthquake, and the SJFT earthquake are 10.3, 15 (width-limited), and 2.8 km ($w = L$), respectively. The estimated stress drops are then about 0.3, 3.7, and 0.3 MPa, respectively. These values are slightly lower than those in previous studies (Wen *et al*. 2014; Lee *et al*. 2015; Ross & Ben-Zion 2016; Yagi *et al*. 2016), but still within a reasonable range considering the large uncertainties in stress drop estimates. More importantly, the derived stress drops here have taken directivity into account and do not rely on corner frequency estimates that depend on azimuth and source models (Kaneko & Shearer 2015). The derived source parameters such as fault length, rupture velocity, and stress drop can provide valuable data for studying the physics of earthquakes (Kanamori & Rivera 2004).

In comparison, the second moment method is another well-developed means of utilizing the second-order expansion of the moment tensor to capture overall characteristics of the spatiotemporal rupture distribution (Backus 1997a,b; McGuire *et al*. 2001, 2002; Chen *et al*. 2005). Its inversion scheme is, however, implemented in the frequency domain rather than in the time domain as in our method. One advantage of the second moment method, compared to ours, is that it provides the additional fault width estimates; but it can only measure the characteristic dimensions (length and width) of a rupture and these are always smaller than the actual dimensions (McGuire *et al*. 2002). Schematically, Fig. 10 illustrates the differences in spatiotemporal resolution of the rupture process between the finite-fault method, the second moment method, and our method. We assume that finite fault inversion gives the best (complete) spatiotemporal recovery of the rupture process, that is slip pattern (Fig. 10a); the second moment method describes a Gaussian-like slip distribution with characteristic dimensions in space and time (Fig. 10b). In contrast, our DMT method using multiple-time-window inversion and a point source assumption can better deal with complicated time evolution of slip (blue triangles), although spatial resolution is restricted along the rupture direction (Fig. 10c). In this sense, Fig. 10(d) gives an explanation for why we underestimate rupture velocity in all synthetic tests since we approximate a continuous linear rupture by a number of subevents with finite source durations (horizontal bars). Thus, although the rupture velocity is set to 2.8 km s^{-1} for the beginning of each subevent (dotted black line), the inversion tends to derive an average rupture velocity calculated from the origin time and the epicenter as shown by the green line, which will always be lower than the input rupture velocity. That is, the shorter the duration of subevents is (i.e. rise time), the more accurate the inverted rupture velocity that is obtained.

While we perform a moment tensor inversion before the directivity inversion in this study, focal mechanism solutions from the first step could always be taken from existing catalogs, previous studies, or various agencies. Once the directivity inversion is performed, rupture properties such as rupture direction, rupture velocity, source duration, and in turn rupture length and stress drop could be rapidly obtained. We have demonstrated that even with simple 1-D velocity models, this method could apply to a range of earthquakes (M_w 4.7–7.0) with satisfactory results. More advanced 3-D velocity models and EGF approaches could be incorporated in the scheme to improve higher frequency waveform modeling for smaller magnitude earthquakes. The addition of a directivity search to typical moment tensor inversion is easily implemented and thus has potential to be automated in real-time moment tensor monitoring systems (Tsuruoka *et al*. 2009; Ekstrom *et al*. 2012; Lee *et al*. 2013). Applying this method to a range of earthquakes could provide insights into earthquake mechanisms and physics such as rupture behavior and scaling relations of rupture velocity and stress drop.

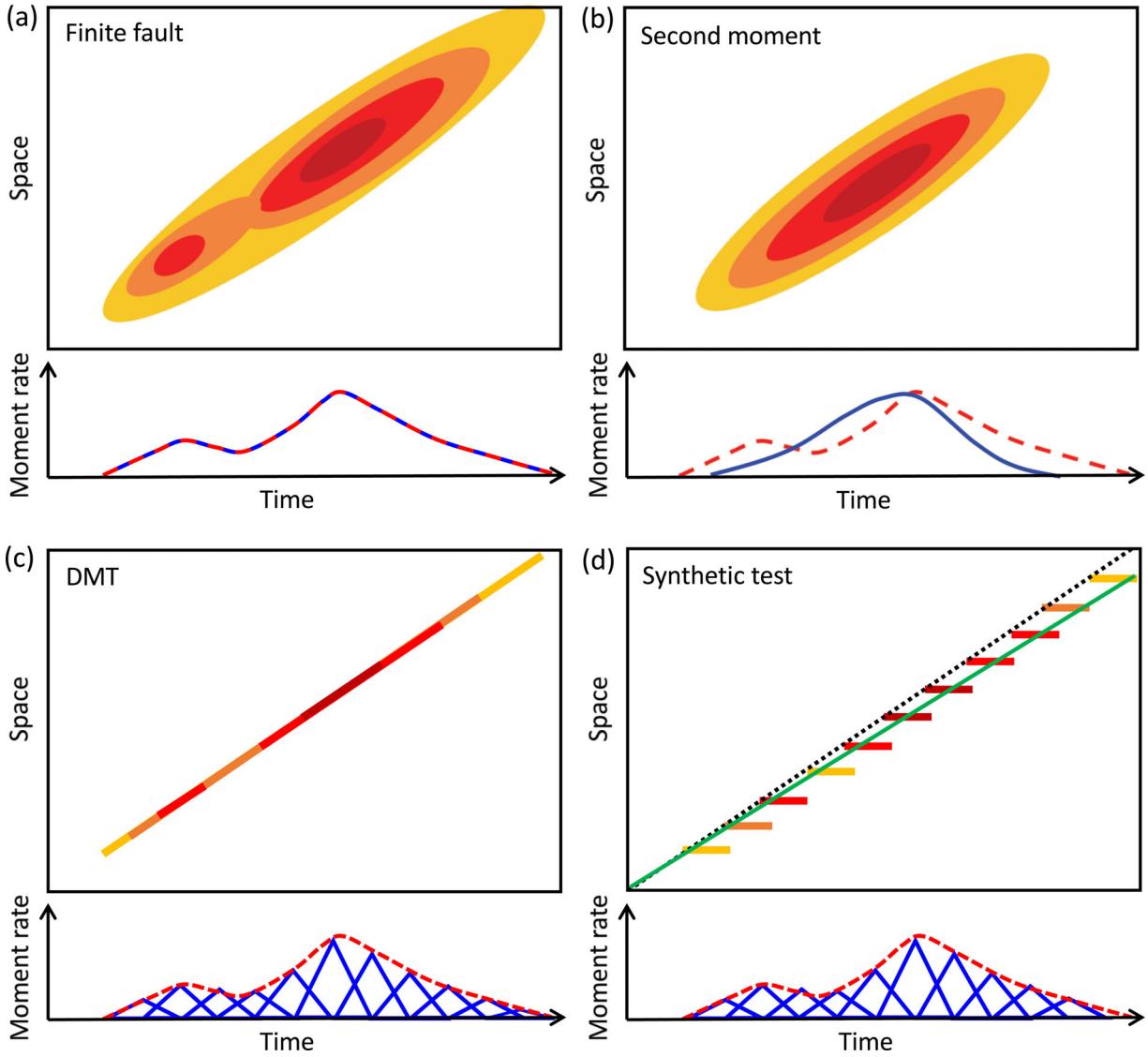

Figure 10. Schematic diagram demonstrating the spatiotemporal slip distribution (upper panels) and source time function (lower panels) derived from (a) finite fault inversion, (b) the second moment method, (c) the directivity moment tensor (DMT) inversion and (d) the DMT synthetic test. The slip patterns in space and time are denoted by warm colors, with warmer color representing larger slip. The actual source time function and estimated source time functions are indicated by dashed red and solid blue curves/triangles, respectively. The slopes of the dotted black and solid green lines in (d) denote the input and inverted rupture velocities, respectively, which explain the underestimate of rupture velocity in the synthetic tests (refer to Section 3).

ACKNOWLEDGEMENTS

We thank Zachary Ross, Lingling Ye, and Zhongwen Zhan for helpful discussion. We also thank Carl Tape and an anonymous reviewer for their constructive comments. The seismic data used in this study were obtained from the Broadband Array in Taiwan for Seismology (IESAS 1996), National Research Institute for Earth Science and Disaster Resilience (F-net), and Southern California Earthquake Data Center (SCEDC 2013). This work was partially supported by National Science Foundation grant EAR-1453263 and Ministry of Science and Technology grant 105-2116-M-001–026-MY2. Naofumi Aso was a Japan Society for the Promotion of Science (JSPS) Overseas Research Fellow (2015-146).

REFERENCES

Aki, K., 1966. Generation and propagation of G waves from the Niigata earthquake of June 16, *Bull. Earthq. Res. Inst., Tokyo Univ.,* **44,** 23–88.

Asano, K. & Iwata, T., 2016. Source rupture processes of the foreshock and mainshock in the 2016 Kumamoto earthquake sequence estimated from the kinematic waveform inversion of strong motion data, *Earth Planets Space,* **68,** 147, doi:10.1186/s40623-016-0519-9.

Aso, N. & Ide, S., 2014. Focal mechanisms of deep low-frequency earthquakes in Eastern Shimane in Western Japan, *J. geophys. Res.,* **119,** 364–377.

Backus, G.E., 1977a. Interpreting the seismic glut moments of total degree two or less, *Geophys. J. R. astr. Soc.,* **51,** 1–25.

Backus, G.E., 1977b. Seismic sources with observable glut moments of spatial degree two, *Geophys. J. R. astr. Soc.,* **51,** 27–45.

Beroza, G.C., 1995. Near-source modeling of the Loma Prieta earthquake: evidence for heterogeneous slip and implications for earthquake hazard, *Bull. seism. Soc. Am.,* **81,** 1603–1621.

Boatwright, J., 2007. The persistence of directivity in small earthquakes, *Bull. seism. Soc. Am.,* **97**(6), 1850–1861.

Camanni, G. *et al.*, 2014. Basin inversion in central Taiwan and its importance for seismic hazard, *Geology,* **42**(2), 147–150.

Chen, Y.-L., 1995. Three-dimensional velocity structure and kinematic analysis in the Taiwan area, *PhD thesis*, National Central University, Jungli, Taiwan.

Chen, P., Zhao, L. & Jordan, T.H., 2005. Finite moment tensor of the 3 September 2002 Yorba Linda Earthquake, *Bull. seism. Soc. Am.,* **95**(3), 1170–1180.

Chen, P., Jordan, T.H. & Zhao, L., 2010. Resolving fault plane ambiguity for small earthquake, *Geophys. J. Int.,* **181,** 493–501.

Chuang, R.-Y., Johnson, K.M., Wu, Y.-M., Ching, K.-E. & Kuo, L.-C., 2013. A midcrustal ramp-fault structure beneath the Taiwan tectonic wedge illuminated by the 2013 Nantou earthquake series, *Geophys. Res. Lett.,* **40,** 1–5.

Convertito, V., Caccavale, M., De Matteis, R., Emolo, A., Wald, D. & Zollo, A., 2012. Fault extent estimation for near-real-time ground-shacking map computation purposes, *Bull. seism. Soc. Am.,* **102**(2), 661–679.

Dziewonski, A.M., Chou, T.A. & Woodhouse, J.H., 1981. Determination of earthquake source parameters from waveform data for studies of global and regional seismicity, *J. geophys. Res.,* **86,** 2825–2852.

Ekstrom, G., Nettles, M. & Dziewonski, A.M., 2012. The global CMT project 2004–2010: centroid-moment tensors for 13,017 earthquakes, *Phys. Earth planet. Inter.,* **200–201,** 1–9.

Frez, J., Nava, F.A. & Acosta, J., 2010. Source rupture plane determination from directivity Doppler effect for small earthquakes recorded by local networks, *Bull. seism. Soc. Am.,* **100,** 289–297.

Hadley, D. & Kanamori, H., 1977. Seismic structure of the Transverse Ranges, California, *Geol. Soc. Am. Bull.,* **88** (10), 1469–1478.

Haskell, N.A., 1964. Total energy and energy spectral density of elastic wave radiation from propagating faults, *Bull. seism. Soc. Am.,* **54,** 1811–1841.

Helmberger, D.V. & Engen, G.R., 1980. Modeling the long-period body waves from shallow earthquakes at regional ranges, *Bull. seism. Soc. Am.,* **70**(5), 1699–1714.

Huang, H.-H., Wu, Y.-M., Lin, T.-L., Chao, W.-A., Shyu, J.B.H., Chan, C.-H. & Chang, C.-H., 2011. The preliminary study of the 4 March 2010 Mw6.3 Jiasian, Taiwan, Earthquake Sequence, *Terre. Atmos. Oceanic Sci.,* **22**(3), 283–290.

Ide, S. & Takeo, M., 1997. Determination of constitutive relations of fault slip based on seismic wave analysis, *J. geophys. Res.,* **102**(B12), 27379–27391.

Institute of Earth Sciences, Academia Sinica, Taiwan (IESAS), 1996. *Broadband Array in Taiwan for Seismology,* Institute of Earth Sciences, Academia Sinica, Taiwan, Other/Seismic Network, doi:10.7914/SN/TW.

Ishii, M., Shearer, P.M., Houston, H. & Vidale, J.E., 2005. Extent, duration and speed of the 2004 Sumatra-Andaman earthquake imaged by the Hinet array, *Nature,* **435,** 933–936.

Kanamori, H. & Anderson, D.L., 1975. Theoretical basis of some empirical relations in seismology, *Bull. seism. Soc. Am.,* **65**(5), 1073–1095.

Kanamori, H. & Rivera, L., 2004. Static and dynamic scaling relations for earthquakes and their implications for rupture speed and stress drop, *Bull. seism. Soc. Am.,* **94**(1), 314–319.

Kanamori, H. & Rivera, L., 2008. Source inversion of W phase: speeding up tsunami warning, *Geophys. J. Int.,* **175,** 222–238.

Kanamori, H. *et al.*, 2016. A strong-motion hot spot of the 2016 Meinong, Taiwan, earthquake (Mw = 6.4), *Terr. Atmos. Oceanic Sci.,* **28**(5), doi: 10.3319/TAO.2016.10.07.01.

Kane, D.L., Shearer, P.M., Goertz-Allmann, B.P. & Vernon, F.L., 2013. Rupture directivity of small earthquakes at Parkfield, *J. geophys. Res.,* **118,** 212–221.

Kaneko, Y. & Shearer, P.M., 2015. Variability of seismic source spectra, estimated stress drop, and radiated energy, derived from cohesive-zone models of symmetrical and asymmetrical circular and elliptical ruptures, *J. geophys. Res.,* **120,** 1053–1079.

Kikuchi, M. & Kanamori, H., 1991. Inversion of complex body waves–III, *Bull. seism. Soc. Am.,* **81,** 2335–2350.

Koper, K.D., Hutko, A.R., Lay, T., Ammon, C.J. & Kanamori, H., 2011. Frequency-dependent rupture process of the 2011 Mw 9.0 Tohoku earthquake: comparison of short-period P wave backprojection images and broadband seismic rupture models, *Earth Planets Space,* **63,** 599–602.

Kubo, H., Suzuki, W., Aoi, S. & Sekiguchi, H., 2016. Source rupture processes of the 2016 Kumamoto, Japan, earthquakes estimated from strong-motion waveforms, *Earth Planetes and Space,* **68,** 161, doi:10.1186/s40623-016-0536-8.

Kurzon, I., Vernon, F., Ben-Zion, Y. & Atkinson, G., 2014. Ground motion prediction equations in the San Jacinto fault zone: significant effects of rupture directivity and fault zone amplification, *Pure appl. Geophys.,* **171**(11), 3045–3081.

Lay, T. & Wallace, T.C., 1995. *Modern Global Seismology,* Academic Press.

Lee, S.-J., Ma, K.-F. & Chen, H.-W., 2006. Three-dimensional dense strong motion waveform inversion for the rupture process of the 1999 Chi-Chi, Taiwan, earthquake, *J. geophys. Res.,* **111,** B11308, doi:10.1029/2005JB004097.

Lee, S.-J. *et al.*, 2013. Towards real-time regional earthquake simulation I: real-time moment tensor monitoring (RMT) for regional events in Taiwan, *Geophys. J. Int.,* **196,** 432–446.

Lee, S.-J., Yeh, T.-Y., Huang, H.-H. & Lin, C.-H., 2015. Numerical earthquake models of the 2013 Nantou, Taiwan, earthquake series: Characteristics of source rupture processes, strong ground motions and their tectonic implication, *J. Asian Earth Sci.,* **111,** 365–372.

Leonard, M., 2010. Earthquake fault scaling: self-consistent relating of rupture length, width, average displacement, and moment release, *Bull. seism. Soc. Am.,* **100**(5A), 1971–1988.

McGuire, J.J., Zhao, L. & Jordan, T.H., 2001. Measuring the second-degree moments of earthquake space-time distributions, *Geophys. J. Int.,* **145,** 661–678.

McGuire, J.J., Zhao, L. & Jordan, T.H., 2002. Predominance of unilateral rupture for a global catalog of large earthquakes, *Bull. seism. Soc. Am.,* **92**(8), 3309–3317.

Meng, L., Inbal, A. & Ampuero, J.-P., 2011. A window into the complexity of the dynamic rupture of the 2011Mw 9 Tohoku-Oki earthquake, *Geophys. Res. Lett.,* **38,** L00G07, doi:10.1029/2011GL048118.

Mori, J. & Hartzell, S., 1990. Source Inversion of the 1988 Upland Earthquake - Determination of a Fault Plane for a Small Event, *Bull. seism. Soc. Am.,* **80,** 507–518.

Olson, A. & Aspel, R.J., 1982. Finite faults and inverse theory with applications to the 1979 Imperial Valley earthquake, *Bull. seism. Soc. Am.,* **72**(6A), 1969–2001.

Park, S. & Ishii, M., 2015. Inversion for rupture properties based upon 3-D directivity effect and application to deep earthquakes in the Sea of Okhotsk region, *Geophys. J. Int.,* **203,** 1011–1025.

Ross, Z.E. & Ben-Zion, Y., 2016. Toward reliable automated estimates of earthquake source properties from body wave spectra, *J. geophys. Res.,* **121,** 4390–4407.

Prieto, G.A., Froment, B., Yu, G., Poli, P. & Abercrombie, R., 2017. Earthquake rupture below the brittle-ductile transition in continental lithospheric mantle, *Sci. Adv.,* **3,** doi:10.1126/sciadv.1602642.

Somerville, P.G., Smith, N.F., Graves, R.W. & Abrahamson, N.A., 1997. Modification of empirical strong ground motion attenuation relations to include the amplitude and duration effects of rupture directivity, *Seism. Res. Lett.,* **68,** 199–222.

Southern California Earthquake Data Center (SCEDC), 2013. Southern California Earthquake Center, *Caltech.Dataset,* doi:10.7909/C3WD3xH1.

Spudich, P. & Chiou, B.S.J., 2008. Directivity in NGA earthquake ground motions: analysis using isochrone theory, *Earthquake Spectra,* **24,** 279–298.

Tan, Y. & Helmberger, D.V., 2010. Rupture directivity of the 2003 Big Bear sequence, *Bull. seism. Soc. Am.,* **100**(3), 1089–1106.

Tsuruoka, H., Kawakatsu, H. & Urabe, T., 2009. GRiD MT (gridbased real-time determination of moment tensor) monitoring the long-period seismic wavefield, *Phys Earth Planet Inter*., **175,** 8–16.

Ueno, H., Hatakeyama, S., Aketagawa, T., Funasaki, J. & Hamada, N., 2002. Improvement of hypocenter determination procedures in the Japan Meteorological Agency (in Japanese), *Quart. J. Seis.,* **65,** 123–134.

Velasco, A.A., Ammon, C.J. & Lay, T., 1994. Empirical Green function deconvolution of broadband surface waves: rupture directivity of the 1992 Landers, California (Mw = 7.3), earthquake, *Bull. seism. Soc. Am.,* **84**(3), 735–750.

Wald, D.J. & Heaton, T.H., 1994. Spatial and temporal distribution of slip for the 1992 landers, california, earthquake, *Bull. seism. Soc. Am.,* **84,** 668–691.

Wang, E. & Rubin, A.M., 2011. Rupture directivity of microearthquakes on the San Andreas Fault from spectral ratio inversion, *Geophys. J. Int.,* **186,** 852–866.

Warren, L.M. & Shearer, P.M., 2006. Systematic determination of earthquake rupture directivity and fault planes from analysis of long-period P-wave spectra, *Geophys. J. Int.,* **164,** 46–62.

Warren, L.M. & Silver, P.G., 2006. Measurement of differential rupture durations as constraints on the source finiteness of deep-focus earthquakes, *J. geophys. Res.,* **111,** B06304, doi:10.1029/2005JB004001.

Wen, Y.-Y., Miyake, H., Yen, Y.-T., Irikura, K. & Ching, K.-E., 2014. Rupture directivity effect and stress heterogeneity of the 2013 Nantou Blind-Thrust Earthquakes, Taiwan, *Bull. seism. Soc. Am.,* **104**(6), 2933–2942.

Yagi, Y., Okuwaki, R., Enescu, B., Kasahara, A., Miyakawa, A. & Otsubo, M., 2016. Rupture process of the 2016 Kumamoto earthquake in relation to the thermal structure around Aso volcano, *Earth Planets Space,* **68,** 118, doi:10.1186/s40623-016-0492-3.

Ye, L., Lay, T. & Kanamori, H., 2013. Large earthquake rupture process variations on the Middle America megathrust, *Earth Planet. Sci. Lett.,* **381**, 147–155.

Ye, L., Lay, T., Kanamori, H. & Rivera, L., 2016. Rupture characteristics of major and great (Mw $\geq$ 7.0) megathrust earthquakes from 1990 to 2015: 1. Source parameter scaling relationships, *J. geophys. Res.,* **121,** doi:10.1002/2015JB012426.1.

Yue, H., Lay, T. & Koper, K.D., 2012. En échelon and orthogonal fault ruptures of the 11 April 2012 great intraplate earthquakes, *Nature,* **490**(7419), 245–249.

Zhan, Z., Shearer, P.M. & Kanamori, H., 2015. Supershear rupture in the 24 May 2013 Mw 6.7 Okhotsk deep earthquake: additional evidence from regional seismic stations, *Geophys. Res. Lett.,* **42,** doi:10.1002/2015GL065446.

Zhu, L. & Rivera, L.A., 2002. A note on the dynamic and static displacements from a point source in multilayered media, *Geophys. J. Int.,* **148,** 619–627.